International Journal of Heat and Fluid Flow 102 (2023) 109142

Contents lists available at ScienceDirect

International Journal of Heat and Fluid Flow

journal homepage: www.elsevier.com/locate/ijhff

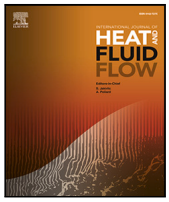

Drag reduction by means of an array of staggered circular cavities at moderate Reynolds numbers

Francesco Scarano [a,b,*], Marc C. Jacob [b], Erwin R. Gowree [a]

[a] Département Aérodynamique et Propulsion (DAEP) ISAE-SUPAERO, Université de Toulouse, 10, avenue Edouard Belin 31400, Toulouse, France
[b] Univ Lyon, Ecole Centrale de Lyon, CNRS, Univ Claude Bernard Lyon 1, INSA Lyon, LMFA, UMR5509, 69130, Ecully, France

ARTICLE INFO

Keywords:
Turbulent boundary layer
Skin friction drag reduction
Hot wire anemometry
Cavities

ABSTRACT

Further insight into the physics of boundary layers developing over an array of circular cavities at moderate Reynolds numbers (Re_θ up to 3400) is gained from hot wire boundary layer surveys on a range of parameters. The findings are consistent with literature as to the possibility of reducing skin friction drag with circular perforations. The results evidence a modification of the mean velocity profile, an increase of the wake parameter and the shape factor associated to a decrease of the skin friction. The modifications of the boundary layer as well as the skin friction reduction are more pronounced when the open area ratio is increased, which is achieved by increasing the cavity diameter or equivalently by decreasing the inter-cavity spacing. The turbulent activity is shifted in the upward direction, the burst intensity decreases in the buffer layer ($10 < Y^+ < 35$) and increases in the upper part of the logarithmic region/beginning of outer layer ($80 < Y^+ < 200$) with the formation of an outer peak in the turbulence intensity profile. The premultiplied spectra and the streamwise shear stress profiles evidence an energy surplus in the same part of the boundary layer and for the highest open area ratios a "bi-hump" behaviour. The formation of outer quasi-streamwise rollers is believed to be the cause of this energy hump in the spectrum. The turbulence statistics show a striking similarity with the turbulent boundary layer in presence of wall-normal blowing. It is believed that the cavities promote a vertical velocity component that displaces the turbulent activity towards the outer region. Different hypotheses to explain the modification of the flow statistics are detailed in the paper.

1. Introduction

The control of turbulent skin friction drag is a crucial task with significant importance both in aerial and ground transportation, where minimising the skin friction drag has a direct impact on greenhouse gas emissions (Ricco et al., 2021; Leschziner, 2020), as well as in the design of thermal insulators and heat exchangers. The turbulent skin friction drag is a consequence of the turbulent boundary layer developing over a surface.

Skin friction drag reduction techniques started to gain interest in the 80's. The majority of the techniques are based on the modification of the turbulent coherent structures and the consequent disruption of the near wall turbulent cycle. This usually manifests in the attenuation of the turbulent activity (namely sweep ($u > 0$, $v < 0$) and ejections ($u < 0$, $v > 0$) altogether known as bursts) and the consequent reduction of the Reynolds shear stress. Techniques such as riblets (Garcia-Mayoral and Jimenez, 2011), and spanwise wall oscillations (Marusic et al., 2021) have proven to be effective in reducing skin friction. The riblets hinder the spanwise movement of the quasi-streamwise vortices, the main mechanism responsible for the bursting activity, and have a characteristic size (spacing and height) ranging from 10 to 20 viscous units (ν/U_τ, where U_τ is the friction velocity). The spanwise wall oscillations technique consists in imposing a spanwise modulation of the flow with a wavelength ranging from 200 to 8000 wall units. The sinusoidal modulation of the spanwise flow imposed by the wall movement tilts the quasi-streamwise vortices, this reduces the occurrence and intensity of the near wall events. The consequence is an attenuation of the turbulent activity thus a skin friction reduction. The practical implementation of the spanwise oscillations, in both real and laboratory conditions, is limited by the high complexity of the setup and the need for an active forcing device (Auteri et al., 2010; Marusic et al., 2021).

Another strategy to reduce the turbulent skin friction drag relies on the skin friction decomposition called FIK equation (Fukagata et al., 2002). A skin friction reduction is possible by enhancing the wall-normal convection term overcoming an increase of Reynolds shear stress. The quasi-streamwise vortices are thus displaced in the upward

* Corresponding author.
E-mail address: fr.scarano@gmail.com (F. Scarano).

https://doi.org/10.1016/j.ijheatfluidflow.2023.109142
Received 14 January 2023; Received in revised form 13 April 2023; Accepted 16 April 2023
Available online 29 April 2023

direction which leads to a modification of the mean flow and a consequent skin friction reduction. This approach has been successfully put into practice by the wall-normal blowing technique (the magnitude is usually about 0.1% of the free-stream velocity) that is found to lead to a considerable skin friction reduction both in numerical simulations (Kametani et al., 2015) and experiments (Kornilov, 2015; Hwang and Biesiadny, 1997). The modifications of a turbulent boundary layer subjected to a wall-normal blowing are very similar to what is found for adverse pressure gradient (APG) turbulent boundary layers (Kornilov, 2015).

The most detectable features in an APG as well as in turbulent boundary layer subjected to wall-normal blowing is the amplification of the wake region of the mean velocity profile. The wake strength, defined using the Coles wake parameter, grows monotonically with the pressure gradient. Others characteristics are the increase of the shape factor H (defined as the displacement to momentum thickness ratio) and, most importantly, the redistribution of energy in the turbulent boundary layer from the near-wall to the outer region. The amplification of the energy associated to the large scale motion is responsible for the rise in turbulent intensity through the entire flow and especially in the outer region with the clear formation of a second peak in addition to the near-wall peak. An increase of the Reynolds shear stress can be observed as well Inoue et al. (2013). The extension of the logarithmic region is reduced up to a point where almost no logarithmic region is noticeable. However, for moderate APGs, the Clauser's chart technique (Kendall and Koochesfahani, 2008) still gives accurate values of the friction velocity (Monty et al., 2011).

Recent studies conducted on large dimples (van Nesselrooij et al., 2016) (diameters up to four times the boundary layer thickness) and cavities (Bhat et al., 2021; Silvestri et al., 2017; Gowree et al., 2019; Scarano et al., 2022b) (diameter in wall units $140 < d^+ < 245$) demonstrated the possibility of obtaining a significant turbulent activity reduction at certain Reynolds numbers. So far, the underlying mechanism is not completely clear and it is sometimes associated with a passive jetting phenomenon (especially when the cavities are connected to a backing cavity) that damps the wall normal velocity fluctuations reducing the Reynolds shear stress (Bhat et al., 2021). Alternatively the property of an array of orifices to absorb turbulent activity (bursts) in a similar manner as they absorb acoustic fluctuations is another candidate mechanism (Silvestri et al., 2017). However, Gowree et al. (2019) showed that the skin friction drag benefit persists in the absence of backing cavities. The LES results reported by Scarano et al. (2022b) showed the presence of a couple of counter-rotating vortices inside the cavities that generate a passive spanwise modulation of the flow that resembles the steady version of the spanwise wall oscillations proposed by Viotti et al. (2009). A similar explanation was proposed by van Nesselrooij et al. (2016) to explain the drag reduction in presence of dimples.

Passive skin friction reduction techniques such as cavities and dimples are preferred to wall-normal blowing and spanwise wall oscillations as they do not require any additional system which would lead to an increase in the overall weight and energy consumption offsetting the gain. The staggered cavity arrangement proposed by Gowree et al. (2019) and Scarano et al. (2022b) is preferable as it should be less susceptible to moderate yaw angles and easier to manufacture. However, the effect of geometrical parameters such as the diameter and the spacing between the cavities is still debatable and it has not been studied in depth so far. In addition, a parametric study addressed in the current work, should provide a clearer picture of the mechanism involved in the skin friction reduction. In the following section the experimental set-up and parameter range are described. The main results are presented in Section 3 whereas Section 4 is dedicated to a discussion about the turbulent activity, the article is concluded by an additional discussion with final remarks.

Table 1
Flow parameters for the three different test conditions, baseline case.

U_∞ [m/s]	$k_a \cdot 10^{-6}$	δ [mm]	H	Re_θ	Re_τ	U_{τ_0}	l^+
10	0.013	23.2	1.38	1750	620	0.44	42
15	0.005	23.1	1.37	2750	890	0.60	58
20	0.002	22.0	1.36	3430	1090	0.78	74

2. Experimental setup

Accurate boundary layer measurements are conducted in the low speed closed-loop wind tunnel of ISAE-SUPAERO. The same setup was previously used for similar investigations (Scarano et al., 2022b,a).

The test model consists of a 2.5 m long, 1.2 m wide flat plate with an elliptic leading edge and is mounted horizontally. It is equipped with a square insert (400 mm) that can house panels varying from smooth to models with arrays of circular cavities. The insert is located 1.1 m downstream of the leading edge. To trip the laminar boundary layer, a wire is placed right after the flat plate's elliptical leading edge. A close to zero pressure gradient is ensured by the deflection of a flap at the trailing edge of the flat plate (the acceleration parameter is smaller than 10^{-7}). Optical monitoring ensured precise measurements of the probe-to-wall distance (Gowree et al., 2015; Örlü and Alfredsson, 2012). The hot wire anemometry probe, connected to a probe support, is mounted on a traversing system that allows displacements in the normal-to-plate direction (Y) (minimum displacement of 12.5 µm, between 0.35 to 0.61 viscous lengths). A Dantec 55P15 boundary layer hot wire probe is used for the measurements with a sampling frequency of 20 kHz. The length l of the wire in wall units is reported in Table 1. The operating temperature of the wire is around 230°C and the overheat ratio is set to 1.75. Three flow conditions are tested 10, 15 and 20 m/s at which the Reynolds number based on the momentum thickness for the smooth case is $Re_\theta = 1750, 2750$ and 3430 respectively and the corresponding boundary layer parameters are reported in Table 1. Further details about the smooth baseline case can be found in Scarano et al. (2022a).

The perforated models are manufactured in plexiglass to reduce heat transfer between the hot wire probe and the wall. Following Gowree et al. (2019) the back of the perforated model is sealed with rigid aluminium tape in order to avoid interactions between the cavities and the casing gap beneath them. The smooth part upstream of the first row of cavities has been designed to recover an unperturbed turbulent boundary layer after the effect of the small gap between the model and the plate (0.1 mm that has been sealed with tape to avoid leakage). The boundary layer that impinges on the first cavity row has been verified to be fully developed and canonical for all the flow conditions. So the effect of the discontinuity at the leading edge of the model can be neglected (see Fig. 1).

A set of geometrical parameters can be varied: the diameter of the cavity, d, the spacing, L and the height of the perforation, h. The different test models are named in the order by the diameter, the spacing and the height, the values in the name are the dimensions in millimetres. When the height is not specified the values is equal to 4 mm. A derived quantity is the Open Area Ratio (OAR) defined as the ratio between the perforated area and the total area without perforations (excluding the smooth region that surround the perforations). An additional parameter is the alignment of the cavities. For the d6L11 case an additional aligned version of the model, is tested. Testing this model is equivalent to test the classic staggered case with a yaw angle of 45°. For the aligned case, the OAR and the h has been kept constant with respect to the staggered case. Some of the test models are presented in Fig. 2.

Two groups of test cases can be identified: in the first one, the spacing is fixed and the diameter ranges from 3 to 6 mm while in the second group, the diameter is fixed and the cavity spacing L ranges from 7 to 22 mm. The characteristic dimensions in wall units (d^+, L^+, h^+) for the different test cases change with the free-stream conditions; the scaling in inner and outer units of the geometrical parameters are reported

Table 2
Test models, geometrical parameters for the three different test conditions, downstream measurement location, baseline friction velocity used to obtain the values in wall units. An average value of δ =23 mm is used. The colours in the tabular are the same used in the plots.

CASE	d^+			L^+			δ/h	d/h	OAR	Measurements
d3L11	85	115	150	305	425	540	7.7	0.75	0.1168	Z_0, Z_+, Z_-
d4L11	110	155	200	305	425	540	5.7	1.00	0.2077	Z_0, Z_+, Z_-
d5L11	140	190	245	305	425	540	4.6	1.25	0.3245	Z_0, Z_+, Z_-
d6L11	165	230	295	305	425	540	3.8	1.50	0.4673	Z_0, Z_+, Z_-
d6L11h1.5	165	230	295	305	425	540	3.8	0.50	0.4673	Z_0
d6L11h2	165	230	295	305	425	540	3.8	0.77	0.4673	Z_0
d6L11 align	165	230	295	305	425	540	3.8	1.50	0.4673	Z_0
d3L07	85	115	150	195	270	345	7.7	0.75	0.2885	Z_0, Z_+, Z_-
d3L11	85	115	150	305	425	540	7.7	0.75	0.1168	Z_0, Z_+, Z_-
d3L16	85	115	150	445	615	790	7.7	0.75	0.0552	Z_0, Z_+, Z_-
d3L22	85	115	150	610	850	1080	7.7	0.75	0.0292	Z_0, Z_+, Z_-
d3L07h2	85	115	150	195	270	345	7.7	0.75	0.2885	Z_0

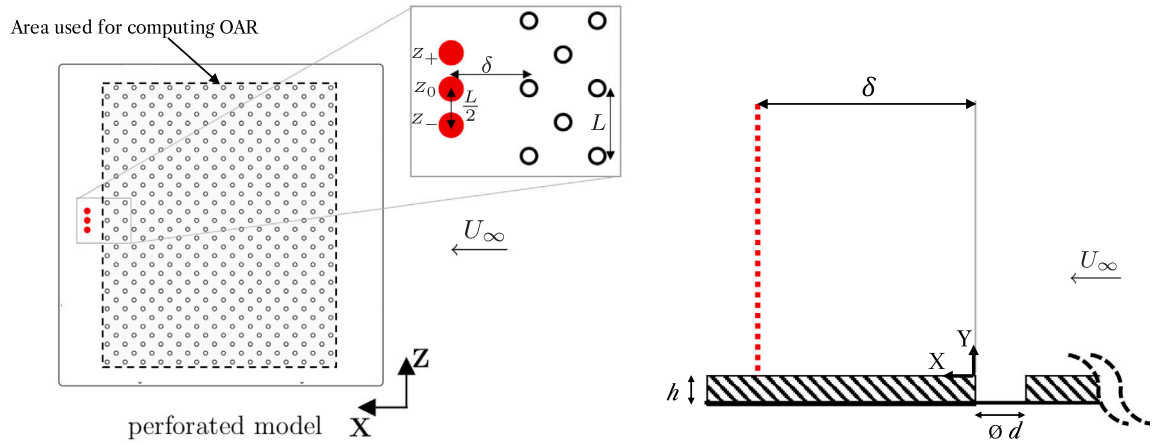

Fig. 1. Example of the test model and downstream measurement location.

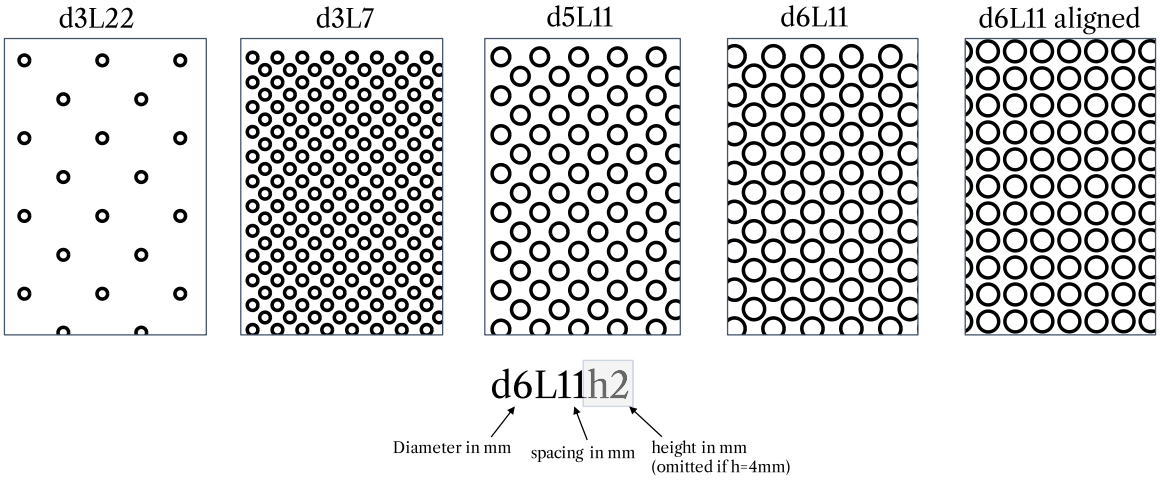

Fig. 2. Cavities arrangement and details of some of the test models.

in Table 2. The friction velocity used to compute the geometrical parameters in wall units is obtained on the baseline smooth surface. In the Table 2 the type and the location of measurements conducted on the model are reported.

Usually, when a turbulent boundary layer control technique that requires the modification of the surface is tested, the measurements are carried out in the downstream part of the controlled surface (Iuso et al. (2002), Silvestri et al. (2017), Choi et al. (1998), Di Cicca et al. (2002), Cafiero and Iuso (2022) to cite a few). The present measurements are therefore conducted approximately one boundary layer thickness downstream of the last row of cavities (about 15δ downstream of the first row of cavities, see Fig. 1), where the boundary layer is expected to be in equilibrium with the non-smooth surface (Antonia and Luxton, 1971).

In order to confirm that the properties of the boundary layer subjected to the perforations are not purely localised along the centreline of a cavity and thus potentially in the wake of the last row of the cavity, further measurements are made at two additional spanwise position. The spanwise spacing is half of the cavity distance L, this way the measurements are in the wake of a cavity (Z_0) between two cavities

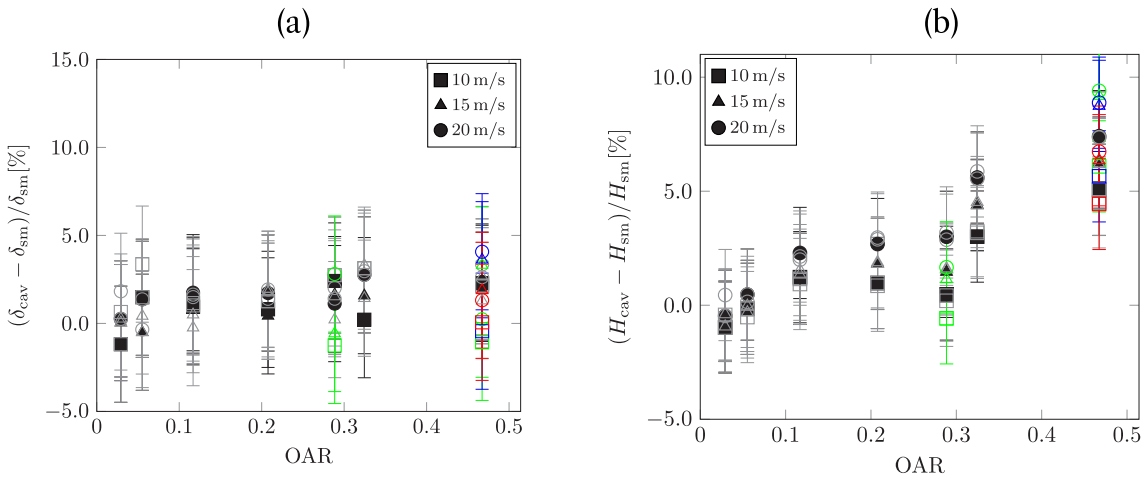

Fig. 3. Boundary layers parameters percentage variation with respect to the smooth baseline case plotted against OAR, (a) boundary layer thickness, (b) shape factor. In black Z_0 measurements, in grey Z_+ and Z_-, in green $h = 2$ and in blue $h = 1.5$, in red the aligned case, bars are the measurement uncertainty. (For interpretation of the references to colour in this figure legend, the reader is referred to the web version of this article.)

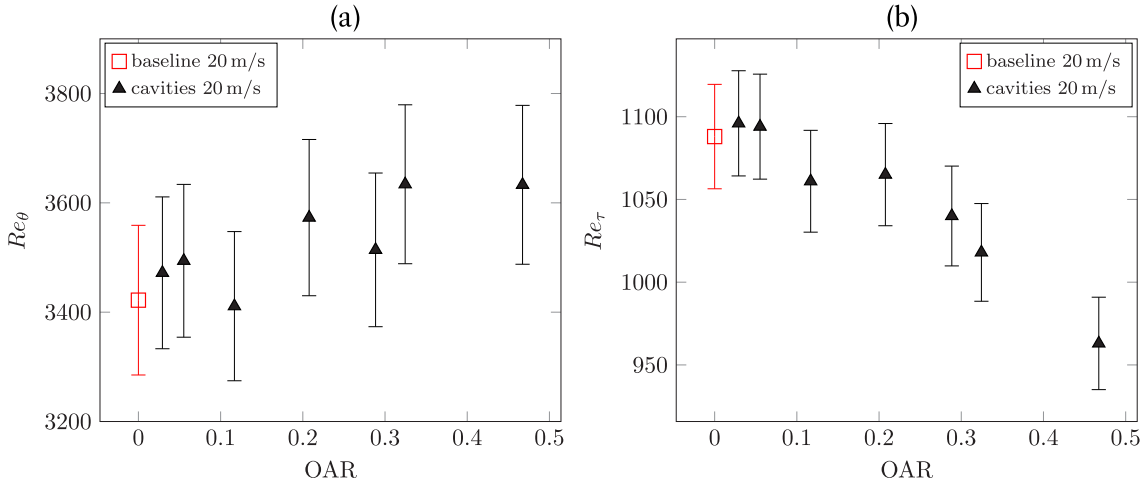

Fig. 4. Momentum thickness based Reynolds number (a) and friction Reynolds number (b) plotted against OAR at 20 m/s, measurement location 1δ downstream of the cavities.

(Z_+ and Z_-). With the exception of the subsection dedicated to the spanwise measurements, the measurements referred to the trailing edge will always be in the wake of the cavity (Z_0).

3. Results

3.1. Turbulent boundary layer statistics and integral parameters

The effects of the perforations on the boundary layer thickness δ and the shape factor H are displayed in Fig. 3. The percentage variation of the different cases with respect to the baseline smooth plate is plotted against the OAR. From Fig. 3 a) no appreciable modification of the boundary layer thickness can be observed as for all the perforated cases the variation with respect to the baseline case is within the uncertainty of the measurement. A mild increase in the shape factor with respect to the baseline case can be noted. The difference is almost within the uncertainty range but there is a systematic increase. For the case with the largest OAR (namely d6L11) an increase of approximately 7% is observed while the effect of the Reynolds number can be considered negligible.

The Reynolds number modification for the measurement position 1δ downstream the last row of cavities at 20 m/s is reported in Fig. 4. It can be seen that the increase of Re_θ and the decrease of Re_τ are more pronounced when increasing the OAR.

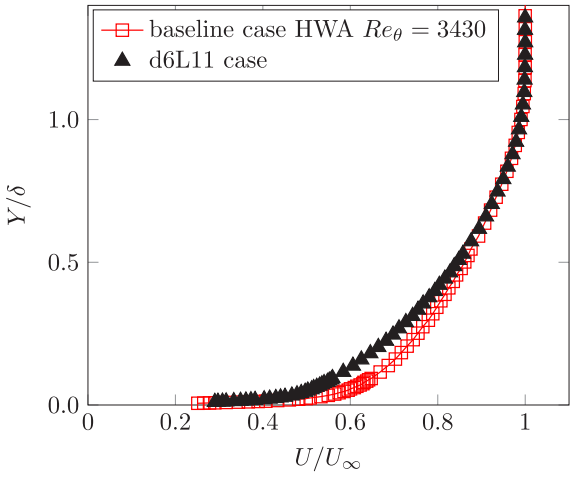

Fig. 5. Mean streamwise velocity at 20 m/s scaled in outer quantities, comparison between baseline case and d6L11.

The modification of the mean velocity profile in outer scales in presence of cavities is plotted in Fig. 5 for the d6L11 case at 20 m/s.

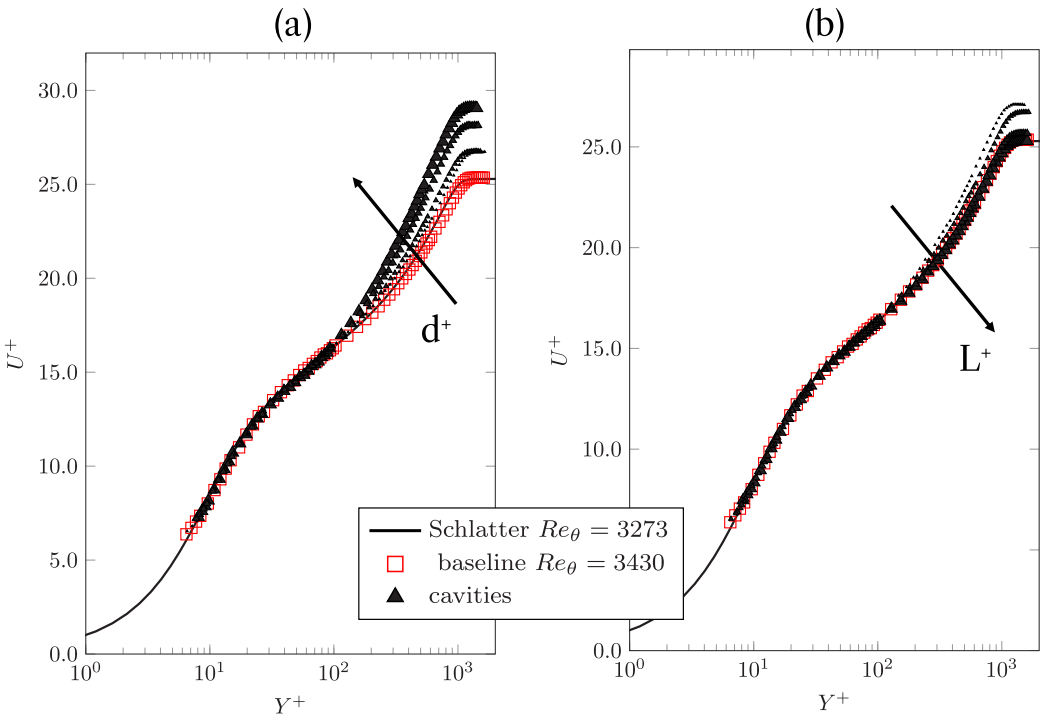

Fig. 6. Mean streamwise velocity in wall units at 20 m/s, actual friction velocity is used. The profiles for the perforated cases are plotted in black using different dimensions for the markers, bigger markers represents larger values of d^+, subfigure (a) or L^+, subfigure (b), and are also indicated by the arrows. Solid lines are the data of Schlatter and Örlü (2010) at similar Reynolds number.

As shown by the shape factor variation in Fig. 3 (b), the profile is less full compared to the smooth baseline case. On Fig. 5 it can be further observed that this is associated with a mean velocity deficit in the region $0.5 < Y/\delta < 0.2$. The mean velocity profiles in wall units at 20 m/s at the measurement location Z_0 are reported in Fig. 6. The friction velocity U_τ is obtained with the Clauser chart technique by a fit of the mean profiles with the Spalding equation (Kendall and Koochesfahani, 2008) with $k = 0.41$ and $B = 5.5$. The actual friction velocity is used to non-dimensionalise all the statistics in inner units. The smooth baseline shows a good match with the numerical results by Schlatter and Örlü (2010). The detailed validation of the baseline case is reported in Scarano et al. (2022a). For the 10 m/s case the friction velocity is evaluated as well using the least square fit technique proposed by Hutchins and Choi (2002). The friction velocity difference obtained with the two techniques lies within the measurement uncertainty. This gives confidence in the application of the Clauser chart technique and justifies the choice of the constants k and B even at the higher free-stream velocity where the least square fit in the viscous sublayer is not possible due to lack of measurement points. The mean velocity profiles exhibit a considerable deviation from the smooth baseline, which is more evident in the wake region. The effect is more pronounced for larger values of d and for smaller values of L. For the largest values of L (cavities furthest apart) the smooth condition is almost retrieved. Similar modifications of the mean velocity profile are reported for boundary layers subjected to APG or wall-normal blowing where the velocity profiles are also observed to be less full.

3.2. Local skin friction

In Fig. 7 the local skin friction difference with respect to the baseline case is plotted against the OAR. A local skin friction reduction is found for almost all the flow conditions; the skin friction reduction increases with d while for the largest L the baseline condition is almost retrieved. The data show an overall decreasing trend which confirms that having a denser array of cavities (increasing the OAR) has a beneficial effect

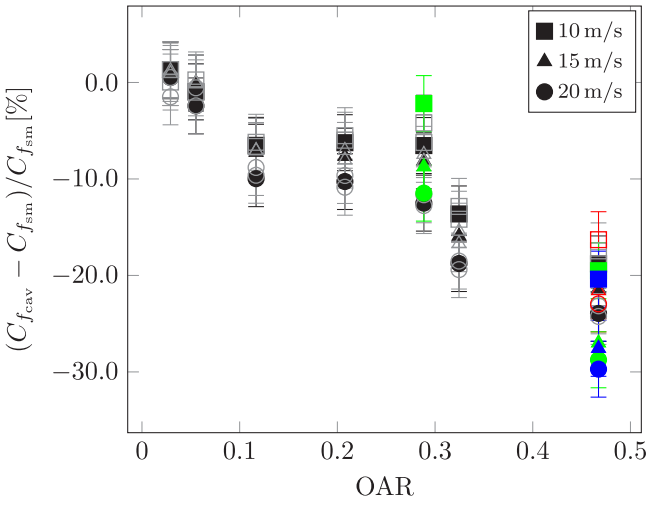

Fig. 7. Local skin friction coefficient variation with respect to the smooth baseline case plotted against the OAR. In black Z_0 measurements, in grey Z_+ and Z_-, in green $h = 2$, in blue $h = 1.5$ and in red the aligned case. (For interpretation of the references to colour in this figure legend, the reader is referred to the web version of this article.)

on the skin friction drag. The results for the spanwise measurements, Z_+ and Z_-, which are reported in grey, lie within the measurement uncertainty taken in wake of the cavity Z_0. Despite the limited number of spanwise measurements, this demonstrates that the skin friction reduction is not just a local artefact but can be considered uniform over the whole cavity pattern along the span. This is further confirmed by the mean and turbulence intensity profiles shown in Fig. 18.

The friction coefficient difference for the aligned case is displayed in red; the results are within the uncertainty suggesting that the cavity orientation has a negligible effect on the performances. The effect of the cavity height is also shown in the Fig. 7, and is further detailed in Fig. 8

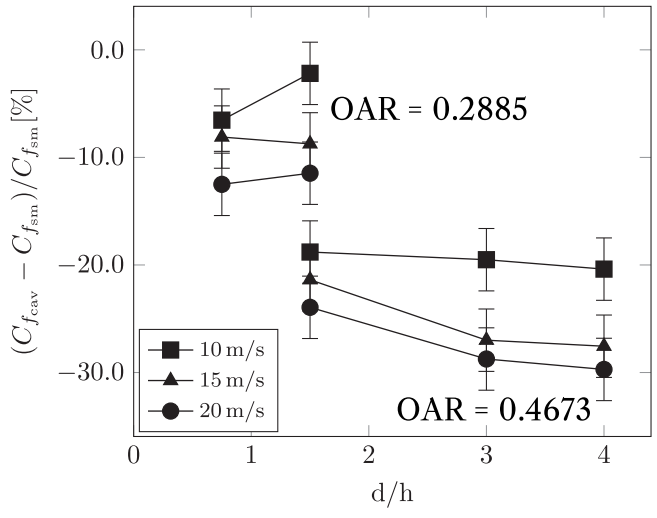

Fig. 8. Local skin friction coefficient variation with respect to the smooth baseline. Effect of the cavity height, h, for two configurations, d3L7 and d6L11 (the OAR value is reported).

where the friction coefficient variation with respect to the baseline case is plotted against the d/h ratio for the d3L11 and d6L11 cases (the relative OAR are specified in the figure). As it can be seen, despite for the d6L11 case, there seem to be a further decrease in the friction coefficient when decreasing the height, that is when increasing the d/h ratio, the variation is within the uncertainty of the measurement. This confirms that the parameter that drives the modification of the friction coefficient, as well as the overall modification of the statistics is the OAR.

As reported by Kendall and Koochesfahani (2008) the Clauser's chart technique relies on the existence of a logarithmic region and of a buffer region if the Spalding equation is used to fit the data. In addition the values of κ and B are imposed *a priori* and this can lead to significant uncertainty in the evaluation of the friction coefficient. As specified above, the values of κ and B have been chosen according to the values obtained with the linear fit in the viscous sublayer for the 10 m/s case.

3.3. Diagnostic function

The diagnostic function $Y^+ \frac{dU^+}{dY^+}$ is shown in Fig. 9 at 20 m/s and the effect of the diameter and the spacing of the perforations is reported in plots (a) and (b) respectively . The logarithmic region can be identified by the range of Y^+ for which the diagnostic function is constant. In Fig. 9 for the baseline case, a narrow logarithmic region can be noted in the range of $50 < Y^+ < 150$ where the diagnostic function reaches the relative minimum. However, an asymptotical logarithmic region, associated to a region of constancy in the diagnostic function, cannot be evidenced due to the moderate Reynolds numbers (it should be present starting from values of $Re_\theta > 4300$ (Schlatter and Örlü, 2010)).

The diagnostic function is almost not affected by the perforations in the inner layer up to $Y^+ \cong 70$, then the diagnostic functions deviate from the baseline case. This deviation is more pronounced for large diameters and small cavity spacing respectively (large diameter and spacing are indicated by thicker lines on the plot and the progression of the curves for increasing values of these two parameters in their respective plot is also indicated by the arrow). The cavities shorten the extension of the logarithmic region and for the larger diameter and the smaller spacing the logarithmic region is hardly identifiable (this is very clear in Fig. 6 (a) and to some extent in Fig. 6 (b)). This, together with the large scatter in the data due to the spatial differentiation (the mean profiles have not been smoothed or interpolated), leads to a even more difficult evaluation of the von Karman constant κ (which is given by the reciprocal of the diagnostic function in logarithmic range) in the configurations with increasing OAR. Similar results are reported by Monty et al. (2011) for turbulent boundary layers subjected to adverse pressure gradients.

3.4. Coles' wake parameter

From the mean velocity profile the Coles wake parameter Π can be evaluated. This parameter is a measure of the wake strength and it is defined as the maximum deviation from the logarithmic law. The outer region can be described by adding the Coles wake function $\mathcal{W}$ to the log law

$$U^+ = \frac{1}{\kappa}\ln(Y^+) + B + \frac{2\Pi}{\kappa}\mathcal{W}(\eta), \quad \eta = Y/\delta \leq 1. \tag{1}$$

At the edge of the boundary layer ($Y/\delta = 1$), $\mathcal{W}(\eta) = 1$, this yields

$$U^+_\infty = \frac{1}{\kappa}\ln(\delta^+) + B + \frac{2\Pi}{\kappa}. \tag{2}$$

In order to compute Π correctly, a precise evaluation of the parameters κ and B of the logarithmic law is needed. This is not trivial for perforated cases because, as mentioned before, it is based on the identification of the logarithmic region that is hardly identifiable in most of the perforated cases. Thus, in the current calculation, the value of $\kappa = 0.41$ is used for all the perforated cases which implies that the wake strength evaluation can be considered only qualitatively. For the baseline case the values of the wake parameters are about 0.32, 0.47 and 0.51. These values are in the range of to the ones reported by Monty et al. (2011) for a larger Reynolds numbers ($\Pi \cong 0.55$ for $Re_\tau = 2800$). The increase in the wake parameter with Reynolds number is reported in literature, however the current values are slightly larger than the ones reported by Chauhan et al. (2009). In Fig. 10 the wake parameter percentage variation with respect to the smooth case is plotted against the OAR. As highlighted from the analysis of the mean velocity profiles in wall units, an overall increase of the wake parameter with the OAR is confirmed by the results of Fig. 10. For the highest OAR the wake strength is almost doubled with respect to the smooth baseline case.

3.5. Skewness

In Fig. 11 the skewness of the streamwise velocity fluctuations is displayed at 20 m/s. It has to be underlined that the effect of the diameter is predominant with respect to the spacing. In fact, despite the d3L7 case having a larger OAR than the d4L11 for instance, only a mild modification of the skewness is observed. A similar skewness increase is found for turbulent boundary layers with an adverse pressure gradient. The skewness has been linked by Mathis et al. (2009) to the amplitude modulation of the small-scale structures, located in the near-wall region, by the large-scales ones. When the cavity diameter widens, the increase in skewness suggests that the large scales enhance the modulation of the small scales. As reported by Monty et al. (2011) for turbulent boundary layers with APG, the effect extends over the whole boundary layer even over the near-wall region when the Reynolds number increases. The current results would then suggest that the influence of large-scales in the near-wall region increases for perforated walls is valid even at lower Reynolds number ($Re_\tau \approx 1000$) compared to the one investigated by Monty et al. (2011) for APG, ($Re_\tau > 2000$).

The discrepancies in the skewness between the baseline case and the numerical results by Schlatter and Örlü (2010) for $Y/\delta < 0.1$ could be due to temporal and spatial hot wires resolution issues (see Örlü and Alfredsson (2012)) or weak "history effects" visible on high order statistics (that can due to tripping devices and a particular leading edge of the flat plate).

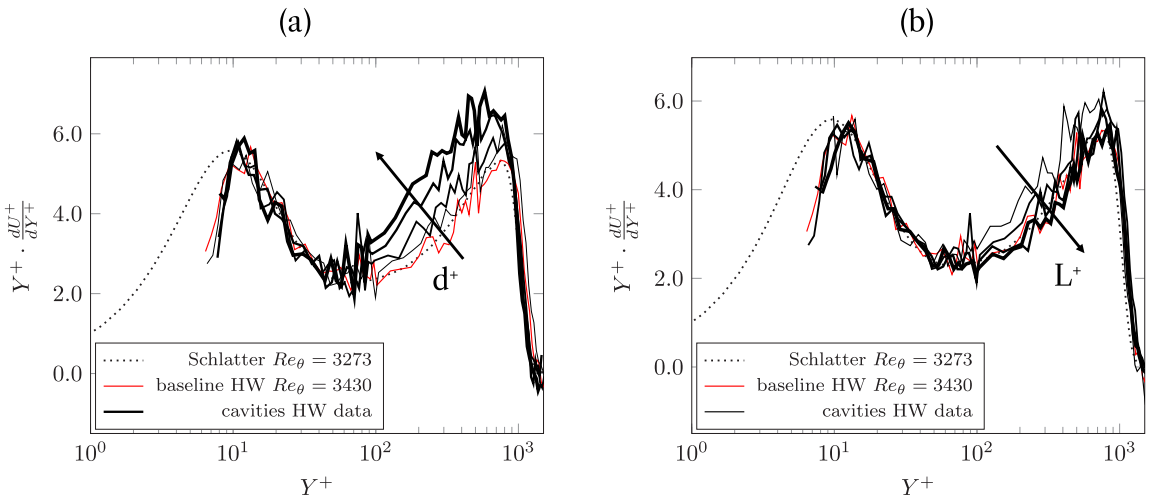

Fig. 9. Diagnostic function at 20 m/s, (a) variation of the diameter d, (b) variation of spacing L. Thicker lines represent increasing of d and L also indicated by the direction of the arrow. Dotted lines are the data of Schlatter and Örlü (2010) at a similar Reynolds number.

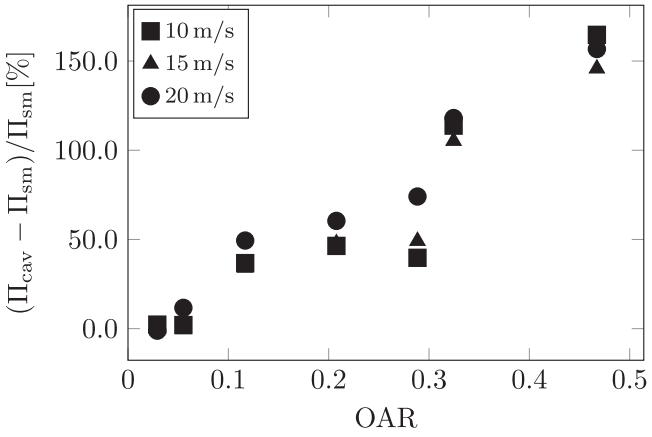

Fig. 10. Coles wake parameter's against OAR.

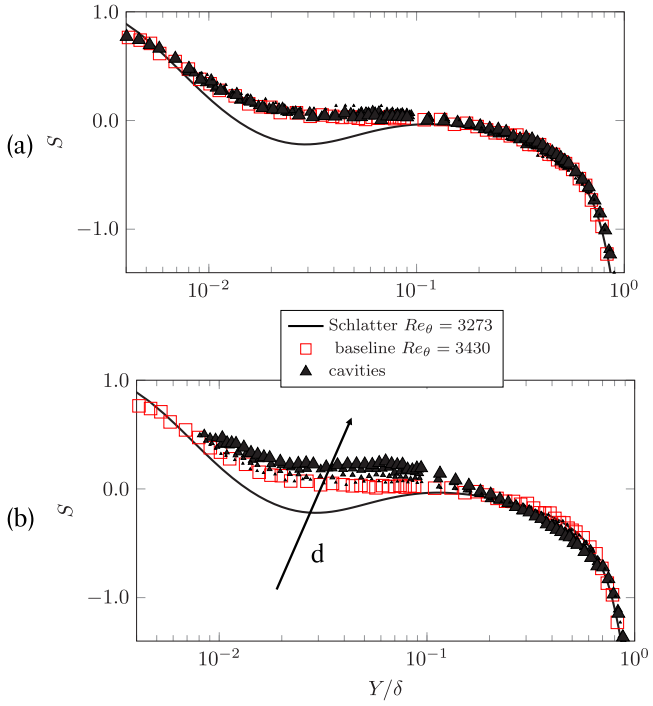

Fig. 11. Skewness at 20 m/s, (a) variation of the diameter d, (b) varaition of the spacing L. Larger markers represent increasing of d and L also indicated by the direction of the arrow. Solid lines are the data of Schlatter and Örlü (2010) at similar Reynolds number.

3.6. Streamwise evolution of the edge velocity

The streamwise evolution of the edge velocity along the perforated region is obtained using the approach proposed by Vinuesa et al. (2017), the results are reported in Fig. 12. For the perforated cases a decreasing trend of the edge velocity can be noted, this indicates indeed the presence of an APG. However, the variation of the edge velocity along the streamwise direction is very modest and it is within the uncertainty of the measurements. The pressure gradient and the acceleration parameter k_a have been calculated. For the 20 m/s case the acceleration parameter is $0.015 \cdot 10^{-6}$ ($\beta = 0.07$) that is about eight times more than the baseline case ($0.002 \cdot 10^{-6}$, see Table 1). Despite this increase, the value is still smaller than $1.6 \cdot 10^{-6}$ prescribed by Patel (1965) as indication for ZPG turbulent boundary layers. It can then be assessed that the perforated surface, despite the similarities in the modification of the statistics, does not generate a significant APG.

4. Modification of the turbulent activity

4.1. Turbulent intensity

The turbulence intensity profiles at 20 m/s are shown in Fig. 13. Similar results, omitted here for brevity, are found for the other flow conditions tested. The baseline case corresponds to a moderate Reynolds number condition for which, in the overlap region, the turbulence intensity decays almost logarithmically and no outer hump is expected. On the contrary, it is clear that the cavities promote an outer hump in turbulence intensity. The presence of an outer peak in the turbulence intensity was reported by Monty et al. (2011) for APG turbulent boundary layers and an increase of the energy in the outer region is typical of turbulent boundary layers with blowing.

4.2. VITA

The Variable Interval Time Averaging (VITA) technique is applied to the profiles. This technique allows the detection of bursts in a turbulent boundary layer (Blackwelder and Kaplan, 1976). The short-term variance is compared to the long-term variance of the entire

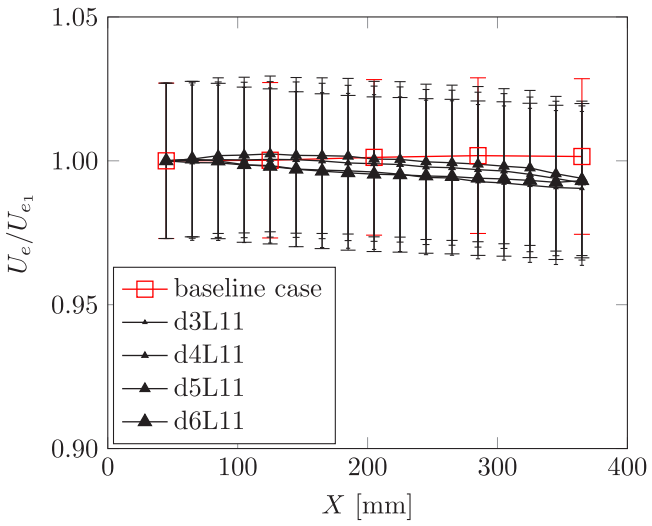

Fig. 12. Streamwise evolution of the edge velocity for three cases at 20 m/s (U_{e_1} is the edge velocity at the first measurement position).

signal. If the short-term variance is larger than the long-term variance multiplied by a user-defined threshold k, a burst is detected (Sullivan and Pollard, 1996). The short-term variance is computed considering a time window that has to be of the same order as the typical passage time of a structure ($T^+ \cong 10$), where $T^+ = \frac{Tu_\tau^2}{\nu}$. Given a fluctuating quantity such as the velocity signal $U(x_i,t)$ the short term average of the variable during a time interval T can be defined as

$$\widehat{U}(x_i,t,T) = \int_{t-\frac{T}{2}}^{t+\frac{T}{2}} U(x_i,s)ds \tag{3}$$

and the short term variance is

$$\widehat{\mathrm{var}}(x_i,t,T) = \widehat{U^2}(x_i,t,T) - [\widehat{U}(x_i,t,T)]^2. \tag{4}$$

The detection is then based on a Heaviside function

$$D(t) = 1 \quad \text{if} \quad \widehat{\mathrm{var}}(x_i,t,T) > k \cdot \sigma_U^2; \quad 0 \quad \text{otherwise} \tag{5}$$

where σ_U^2 is the variance of the entire signal.

The Variable Interval Time Averaging (VITA) technique is applied to the profiles, only the acceleration events, $\frac{\partial U}{\partial t} > 0$, are considered. The friction velocity used to compute the time window as well as the Y^+ is the actual friction velocity for each case. The VITA profiles, namely the intensity, duration and frequency of the bursts (Scarano et al., 2022a) are shown in Fig. 14 for 20 m/s when varying (a) the d, (b) L. The results are obtained for $k = 1$ and $T^+ = 20$ but changing the VITA parameters does not change the considerations reported herein.

In Fig. 14 a major observation is that the shape of the VITA profiles is not dramatically changed by the presence of the cavities. This can be a further indication of the fact that the boundary layer has reached an equilibrium with the perforated surface. An intensity decrease of the local maximum in the region of $10 < Y^+ < 80$ can be noted for the larger diameters and for the narrower spacing. This would confirm that the near-wall cycle is modified by the cavities. Since the wall shear stress decreases (and hence the viscous length-scale increases), the reduction of the inner peak intensity does not correspond to the spatial filtering of the hot-wire probe.

The burst intensity increases with the formation of an outer lobe in the region of $70 < Y^+ < 300$. This result was initially misinterpreted as a manifestation of drag increase by Silvestri et al. (2017) but in fact it can be linked to a shift of the turbulent activity towards the outer layer. In the work of Silvestri et al. (2017) the cavities are not staggered, they are designed to match the dimensions of the coherent structures in a boundary layer with a spacing of 100 viscous units in the spanwise direction and 1000 in the streamwise direction. A decrease of burst intensity at $Y^+ = 100$ is documented up to a certain value of the cavity diameter in wall units ($d^+ = 145$). The explanation given by Silvestri et al. (2017) is that the cavities ingest the sweeps thus reducing the skin friction. According to Silvestri et al. (2017), if the cavities are too large, the shear layer above the cavities breaks, which reduces the drag benefit. As suggested herein using a wider database, the increase in burst intensity at $Y^+ = 100$ is still compatible with a skin friction reduction and can be a manifestation of the upward displacement of the quasi-streamwise vortices and the resulting energy increase in the outer region. A similar mechanism has been reported for wall-normal blowing or APG boundary layers. Similarly to the mean velocity profiles and the turbulence intensity profiles, the effect is more pronounced for large values of d and small values of L that correspond to higher OAR. For small d and large L the smooth intensity profile is almost retrieved.

The burst frequency profile, reported on the centre column of Fig. 14, does not vary with respect to the baseline case when the spacing L is varied. On the contrary for the largest diameters (5 and 6 mm) the frequency of the bursts increases along the entire profiles. In contradiction to the studies of drag reduction by means of large-scale streamwise vortices (Iuso et al., 2002) or spanwise wall oscillations (Di Cicca et al., 2002), the skin friction reduction is not associated with a reduction of the burst frequency

The duration of the bursts, reported on the right column of Fig. 14, decreases along the entire profile for the largest diameters $d = 5$ and 6 mm and is more pronounced in the buffer region where the duration diminishes for all the cases. The duration reduction is stronger for larger diameters and it is barely appreciable for small diameters and when the spacing, L, is increased. The current results suggest that overall the bursting activity is weakened in the buffer region and shifted into the upward direction by the cavities. In fact, in the region $10 < Y^+ < 30$, the bursts are more frequent but weaker and with a smaller duration. In the outer region the same observations apply to the frequency and duration of the larger cavities (d >5 mm), but opposite trends are found for the intensity which grows with respect to the smooth case.

4.3. Spectral content

A similar energy re-organisation of the turbulent boundary layer with a shift towards the outer region can be observed when looking at the premultiplied streamwise velocity spectrum. The spectra are computed using the Welch algorithm with 98 segments with each a window size of 2^{11} samples and no overlap. The two dimensional (2D) premultiplied spectra at 20 m/s for the smooth baseline case and for d3L11, d3L7 and d6L11 cases are shown in Fig. 15.

On the abscissa, the streamwise wavelength in wall units, λ_X^+, is obtained from the time-series by applying Taylor's hypothesis. The ordinate is the normal-to-wall position in wall units. The actual friction velocity is used to non-dimensionalise the spectra and the streamwise wavelength. For the smooth baseline case the inner peak at $\lambda_X^+ \cong 1200$, and $Y^+ \cong 14$, corresponds to the streaks activity as reported by Kline et al. (1967). The inner peak can be observed for all the perforated cases. However, when increasing the OAR, an outer region of high energy in the spectra can be evidenced for the d6L11 case.

In Fig. 16 the isolines corresponding to the contour level of 1.4 of the non-dimensional premultiplied spectra of Fig. 15 are shown for the various diameters (plot a) and spacings (plot b). The thickness of the black lines varies proportionally to the diameter (a) and the spacing (b). It can be noted that an energetic outer region is present for the two cases having the largest OAR. In the figure the mark "+" for the d6L11 and d3L11 cases as well as for the smooth case (in red) identifies the approximate centroid of the high energy region (point of maximum energy). For the d6L11 this maximum is shifted towards lower values of λ_X^+ ($\lambda_X^+ \cong 860$) while changing the spacing only seems to have a limited effect on the streamwise coherence of the streaks, as can be

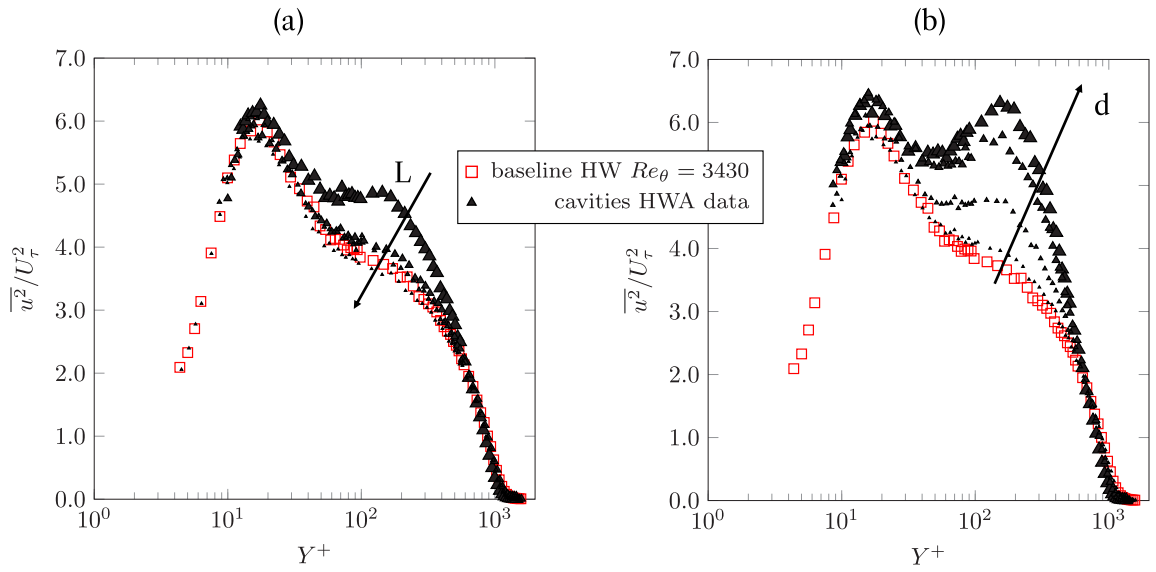

Fig. 13. Turbulence intensity at 20 m/s, (a) effect of the diameter d and (b) effect of spacing L. Size of markers represents the increase in d and L also indicated by the arrow.

seen in Fig. 16 (b), where only a slight shift towards larger Y^+ can be guessed. This suggests that the streaks are shortened by the cavities with the larger diameters. The outer region, located at approximately $Y^+ \cong 150$ is associated with a wavelength of $\lambda_X^+ \cong 1830$. This indicates the presence of elongated outer streaks generated by large diameter cavities while for the other cases an outer peak associated with the contour level of 1.4 is not found. This *double-hump* behaviour revealed by the d6L11 case of Fig. 15, characterises turbulent boundary layers at very high Reynolds numbers ($Re_\tau > 10,000$) it was also reported for rapidly distorted turbulent boundary layers (Diwan and Morrison, 2017).

The contours of the premultiplied spectra difference between the perforated case, d3L11 and d5L11, and the smooth baseline at 20 m/s are shown in Fig. 17. All the spectra are normalised with the smooth baseline friction velocity to better highlight the relative changes in the energy content. The blue parts of the map represent an energy decrease while the red represent an energy increase. As shown for both cases, a decrease in the energy at approximately $Y^+ \cong 15$ associated with a wavelength of about $\lambda_X^+ \cong 1000$, can be clearly distinguished. As this wavelength corresponds to the streamwise spacing of the quasi-streamwise vortices and streaks that are usually located in the buffer layer (centred at $Y^+ \cong 15$), the energy decrease suggests that the streak energy is damped by the presence of the cavities. The energy is shifted towards the outer part of the boundary layer ($Y^+ > 150$), which indicates an upward motion of the quasi-streamwise structures or the formation of outer coherent structures. In addition, especially for the d5L11 case, the energy is spread over a broader range of wavelengths suggesting that a chaotic bursting takes places further upward with respect to the smooth baseline case. Finally the energy transfer is much more intense for larger diameters. Again the results of Fig. 17 confirm that the energy shift towards the outer layer increases with the diameter but it is only weakly affected by the spacing.

It has to be underlined that, due to the limited streamwise extent of the perforated region (approximately 15δ), the flow has not reached an asymptotic state at the measurement location. The adjustment length necessary to reach an asymptotic state is supposed to be linked to the geometry of the cavities (likely the OAR). Future work should focus on the far downstream behaviour and the asymptotic effect of the cavities on a turbulent boundary layer.

5. Discussion and final remarks

It is shown in the present study that an array of circular cavities profoundly influences the boundary layer statistics up to the third order, suggesting that the cavities strongly influence the coherent structures populating the turbulent boundary layer. The increase of the boundary layer thickness is negligible, whereas a moderate increase of the shape factor up to 7% is found. The effect of the cavity diameter, spacing, orientation and height, as well as the Reynolds number are reported. It is further confirmed that the cavities are able to locally reduce the skin friction coefficient by modifying the mean velocity profile. The parameter that governs the skin friction reduction, along with the modification of the statistics and the boundary layer quantities, is the OAR. It can be changed by changing either the diameter or the cavity spacing. The effect of the orientation is negligible. Decreasing the cavity height seems to further improve the performances even if the results are within the uncertainty of the measurements. In the current investigation, the skin friction drag reduction benefit persists for all the conditions tested. The Reynolds number has only a weak effect on the skin friction drag as well on the overall statistics. This negligible effect can be due to the fact that we are dealing with low up to moderate Reynolds numbers. For high Reynolds numbers regimes (say $Re_\tau > 4000$), the effect could potentially become significant.

The spanwise uniformity of the boundary layer modification has been checked confirming that the skin friction reduction is not just a local artefact in the wake of the cavities. The presence of a second peak in the TI and an outer hump in the premultiplied power spectrum at $Y^+ \cong 200$ for the largest OAR, suggests an increase in the energy content of the outer structures and the possible formation of a quasi-streamwise outer rollers and the upward displacement of the streaks.

The modification of the turbulent boundary layer statistics and turbulent activity presented herein evidences striking similarities with wall-normal uniform blowing. As highlighted by Kornilov (2015) there are no reasonable doubts that the modifications undergone by the boundary layer in presence of wall-normal blowing are the same as those in the presence of an adverse pressure gradient. All the modifications of the statistics could then be similarly explained by the formation of a local adverse pressure gradient caused by the circular cavities. An adverse pressure gradient reduces the skin friction but at same time increases the pressure drag contribution (Monty et al., 2011). However, it is demonstrated by the streamwise measurements that the cavities do not generate a significant overall adverse pressure gradient along the measurement domain. For this reason the modification of the boundary layer is expected to be due to a normal-to-wall velocity component generated by the cavities.

The mechanism of skin friction reduction by means of blowing differs from that of the spanwise wall oscillations or the riblets. In fact,

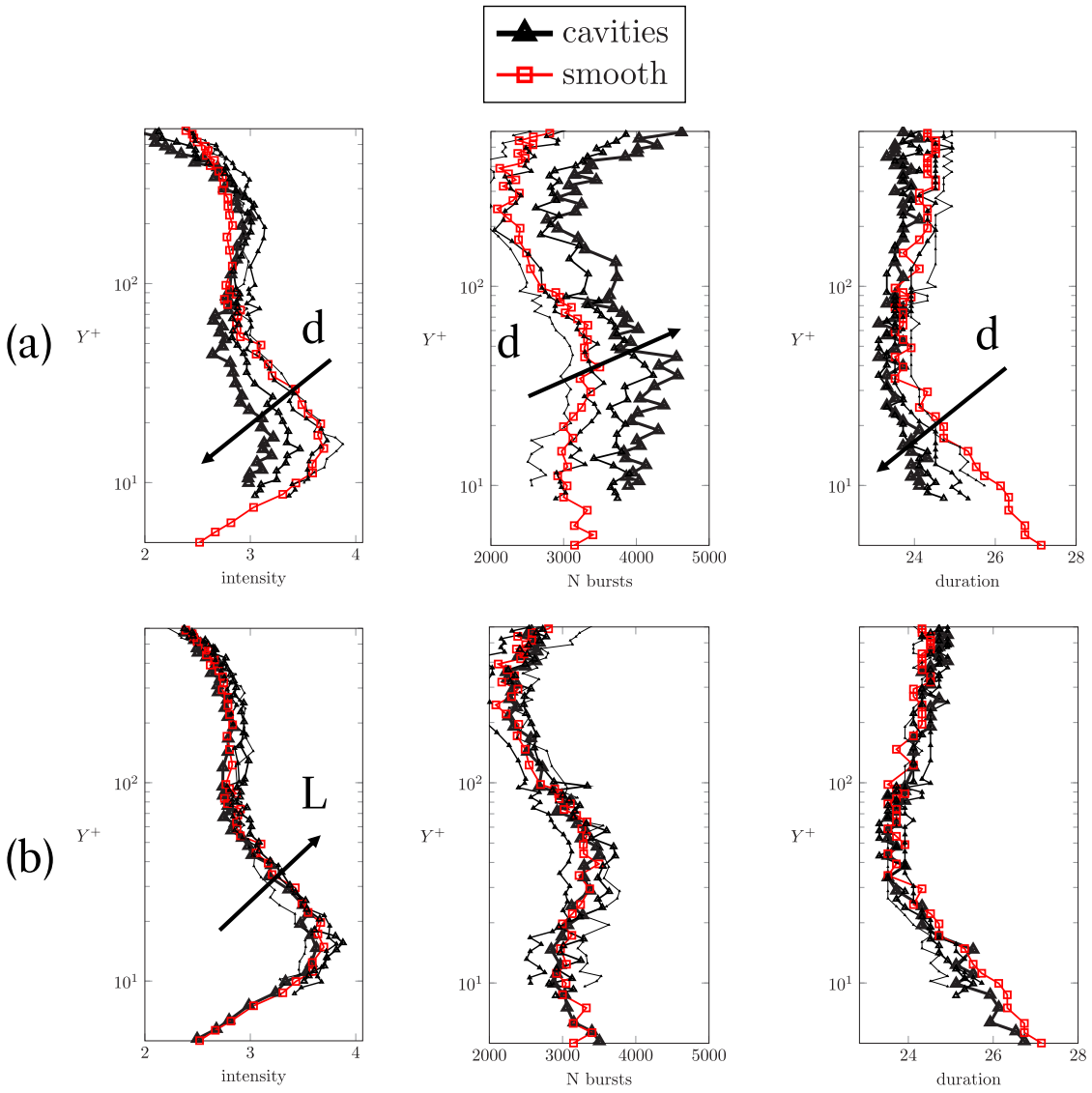

Fig. 14. VITA profiles (acceleration events) at 20 m/s, comparison with smooth baseline case, (a) effect of the diameter d and (b) effect of spacing L. Size of markers represents the increase in d and L also indicated by the arrow, $k = 1, T^+ = 20$.

as mentioned in the introduction, the skin friction reduction is achieved by the modification of the mean wall-normal convection term which overcomes the increase of the turbulent Reynolds shear stress term. The suction acts in the opposite way, it dampens the Reynolds shear stress contribution but increases the mean wall-normal convection leading to a skin friction increase. However, despite the similarities in the results, it is rather difficult to link the unsteady flow inside the cavities to uniform blowing purely from single component HWA measurements. The recirculation inside the cavity and the presence of two counter-rotating vortices documented by Scarano et al. (2022b) does, in fact, not affect the wall-normal mass flow rate. If the cavities created a blowing they would create an equal amount of suction, therefore it is unlikely that the reduction due to the blowing will overcome the increase due to the suction.

A possible explanation is that the blowing process is not created by the recirculating vortex but by the possible presence of shear layer flapping, that comes down to an unsteady blowing effect. This hypothesis is corroborated by the fact that the effect is more pronounced when the perforated area is larger indicating that the extension of this unsteady blowing increases. A similar mechanism has been recently documented by Bhat et al. (2021) who conducted a numerical simulation on a turbulent boundary layer grazing over small orifices backed by a large cavity. They postulated that the backing cavity played an important role. Despite the mean velocity flux through all holes being negligible, instantaneous upward and downward components through the holes were reported. According to the authors, the direction of the wall-normal flow would then be influenced by the structures immediately above the cavities, resulting in an unsteady normal-to-wall component with zero mass flow rate that displaces the quasi-streamwise vortices in the upward direction. The energy increase in the outer region and the formation of a second hump in the burst intensity and in the streamwise shear stress observed in the present study can in fact be explained by a lift-up of the quasi-streamwise vortices that eventually break-up in a strong ejection event of low momentum fluid. The upward displacement of these structures, that carry low momentum fluid, would then modify the mean velocity in such a way that the skin friction would be reduced. A similar mechanism was reported by Kornilov (2015) for wall-normal blowing. It is important to underline that, according to the current results, the presence of a backing cavity is not fundamental to produce the friction drag reduction in contradiction to what was stated by Bhat et al. (2021).

Since the pioneering study by Nikuradse (1930), a rough wall is known to induce secondary wall-normal flow. The source of the secondary flow is ascribed to a local spanwise flow heterogeneity that

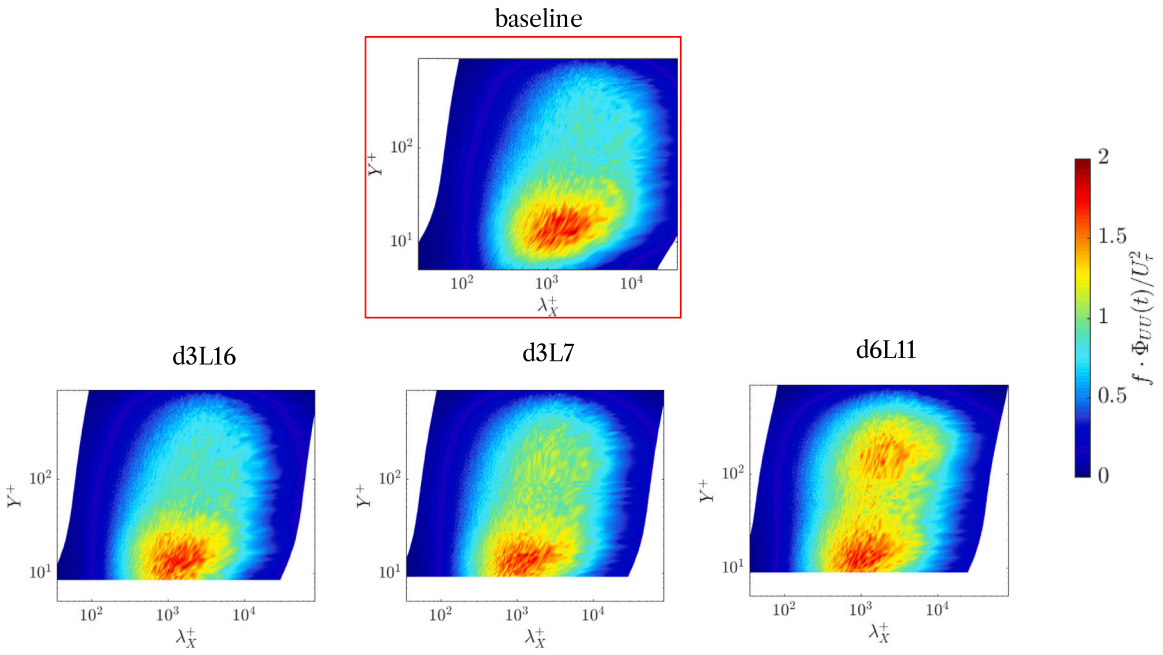

Fig. 15. 2D premultiplied power spectra, comparison between baseline case and some perforated models at 20 m/s. Actual friction velocity is used.

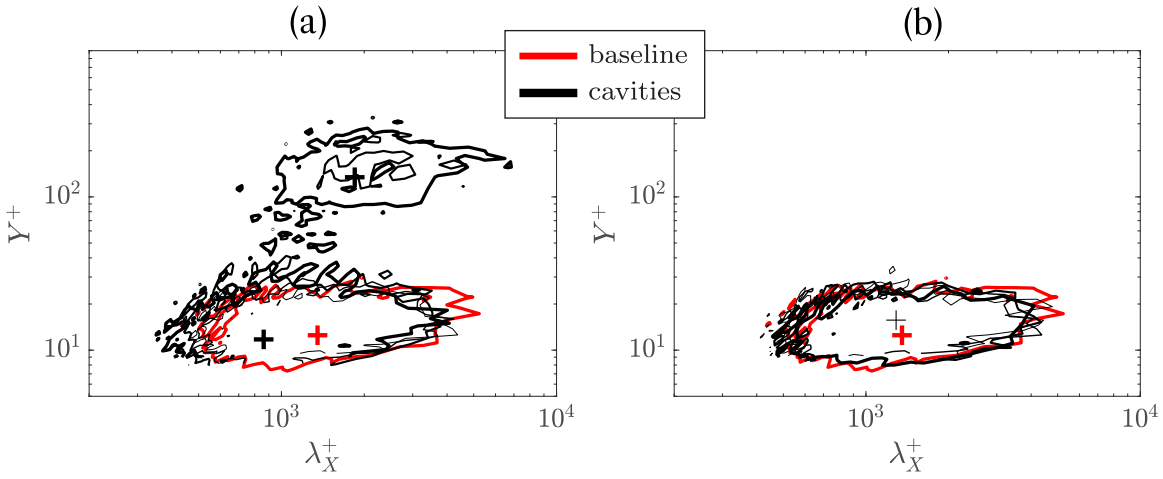

Fig. 16. Isoline of the premultiplied spectra at 20 m/s, (a) effect of d and (b) effect of L. Thicker lines indicate the increase of d and L respectively. Contour level of $f\Phi_{UU}/U_\tau^2 = 1.4$, the point of the relative maximum of the premultiplied spectrum is indicated by the "+" for the baseline case (in red) and in (a) for the d6L11 and (b) d3L7. (For interpretation of the references to colour in this figure legend, the reader is referred to the web version of this article.)

introduces gradients in the Reynolds shear stress distribution (Kadivar et al., 2021). To maintain the balance between turbulence production and dissipation rates, local streamwise vorticity is generated (Hinze, 1967). The streamwise vorticity is associated to the formation of large-scale streamwise rollers that enhance low momentum upwelling motion. The secondary flow then enhances the flow mixing and plays a significant role in the heat transfer enhancement. The type of roughness that generate a secondary flow are the "ridge type roughness" and the "strip-type roughness". Ridge type roughness is defined as spanwise variations of the local elevation of the wall (Stroh et al., 2020) and has been shown to lift the large scale vortices from the near wall region reducing the skin friction and increasing the heat transfer (Soleimani and Eckels, 2021). Perforated walls as the ones studied herein intrinsically have a spanwise heterogeneity in the surface with different surface elevations and it has been shown how they generate a spanwise flow pattern (Scarano et al., 2022b). The presence of a secondary flow with an upwelling motion leading to the formation of quasi-streamwise outer vortices similarly to what happens over ridge-type and strip-type roughness could indeed also explain the modification of the statistics and the spectra.

As stressed by Kornilov (2015), evaluating experimentally the pressure drag penalty associated with wall-normal blowing in a turbulent boundary layer is a complicated task. Hwang and Biesiadny (1997) underline that a total drag reduction is possible if the skin friction reduction overcomes the pressure drag penalty. In a recent paper by Mourão Bento et al. (2022) the flow topology inside a circular cavity shows a pressure force acting on the downstream edge that is due to the impingement of the boundary layer. Hwang and Biesiadny (1997) tested different active normal-to-wall blowing configurations on an airfoil (different OAR, diameters and mass flow rate) and measured the total drag with a force balance. They found that total drag reduction is achievable up to the condition where the blowing generates an inflection of the streamwise mean velocity profile. As for the current case the shape factor increase is computed to be less than 7%, the mean velocity profiles are far from those encountered at separation.

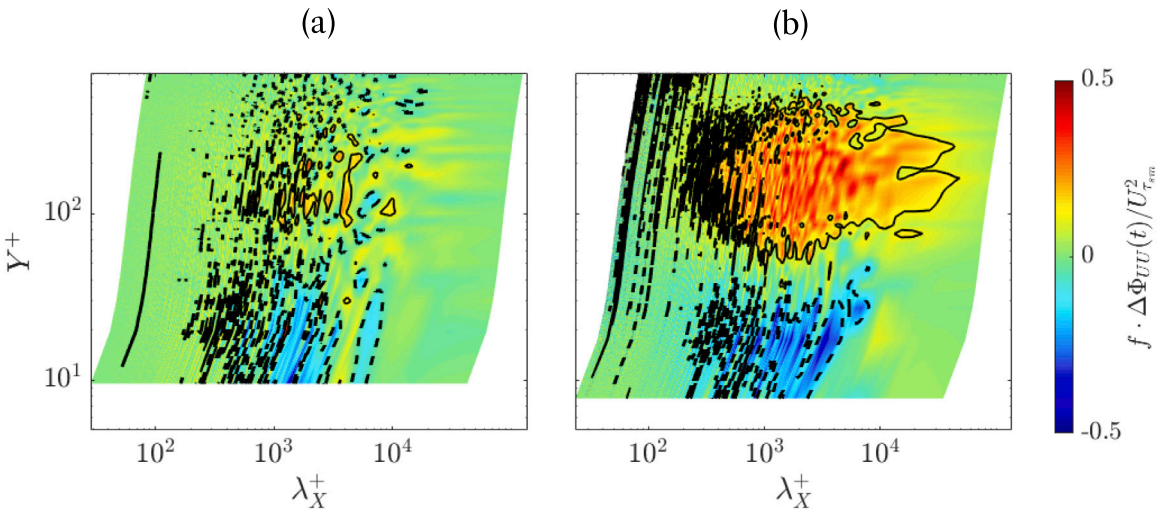

Fig. 17. 2D premultiplied power spectra difference with the smooth baseline case at 20 m/s, (a) d3L11, (b) d5L11. Baseline friction velocity is used.

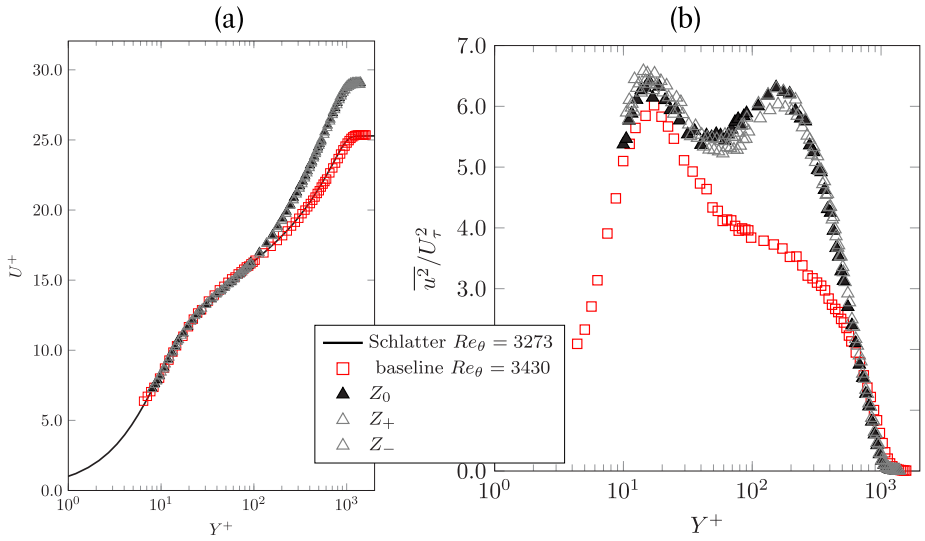

Fig. 18. Effect of spanwise measurement location on (a) mean streamwise velocity profile, (b) turbulence intensity profile, d6L11 at 20 m/s.

Since the pressure drag penalty is not measured directly in the current investigation, the skin friction reduction results presented in Fig. 7 (with values as high as 18%) have to be taken with care and are surely not fully representative of the total drag reduction on the surface. However, the energy increase and the mixing enhancement in the outer region associated to the presence of outer quasi-streamwise rollers can be advantageous for convective heat transfer augmentation applications. The current promising results have to be straightened by force balance measurements or pressure drop measurements in a channel or a pipe. These investigations are the only capable to guarantee the estimation of the net total drag saving by means of cavity arrays that includes the pressure drag increase. Further studies will have to explore a wider range of Reynolds numbers, where the Reynolds number effect might become significant, in order to extend the application range of the current setup. The near wall region on top of the cavities should be carefully studied with techniques such as μ-PIV. A full DNS of the activity inside the cavity is necessary to better understand the flow topology and confirm the hypotheses drawn here.

CRediT authorship contribution statement

Francesco Scarano: Conceptualization, Methodology, Validation, Formal analysis, Investigation, Data curation, Writing – original draft, Writing – review & editing, Visualization. **Marc C. Jacob:** Supervision, Funding acquisition, Project administration, Writing – review & editing. **Erwin R. Gowree:** Supervision, Funding acquisition, Project administration, Writing – review & editing.

Declaration of competing interest

The authors declare that they have no known competing financial interests or personal relationships that could have appeared to influence the work reported in this paper.

Data availability

Data will be made available on request.

Acknowledgements

The research leading to these results received funding from AID (Agence Innovation Défense) under Grant Agreement No 2019 65 0028 for the FriDa project.

Appendix. Spanwise homogeneity

The effect of the measurement locations Z_+ and Z_- with respect to Z_0 is shown in Fig. 18 only for the case *d6L11* but similar results are found for all the cases tested. From the mean and standard deviation streamwise velocity profiles in Fig. 18, no significant differences can be observed in the profiles from the 3 spanwise measurement stations (Z_0, Z_+, Z_-).

References

Antonia, R.A., Luxton, R.E., 1971. The response of a turbulent boundary layer to a step change in surface roughness Part 1. Smooth to rough. J. Fluid Mech. 48 (4), 721–761. http://dx.doi.org/10.1017/S0022112071001824.

Auteri, F., Baron, A., Belan, M., Campanardi, G., Quadrio, M., 2010. Experimental assessment of drag reduction by traveling waves in a turbulent pipe flow. Phys. Fluids 22 (11), 115103. http://dx.doi.org/10.1063/1.3491203.

Bhat, S.S., Silvestri, A., Cazzolato, B.S., Arjomandi, M., 2021. Mechanism of control of the near-wall turbulence using a micro-cavity array. Phys. Fluids 33 (7), 075114. http://dx.doi.org/10.1063/5.0051375.

Blackwelder, R.F., Kaplan, R.E., 1976. On the wall structure of the turbulent boundary layer. J. Fluid Mech. 76 (1), 89–112. http://dx.doi.org/10.1017/S0022112076003145.

Cafiero, G., Iuso, G., 2022. Drag reduction in a turbulent boundary layer with sinusoidal riblets. Exp. Therm Fluid Sci. 139, 110723. http://dx.doi.org/10.1016/j.expthermflusci.2022.110723, URL https://www.sciencedirect.com/science/article/pii/S0894177722001236.

Chauhan, K., Monkewitz, P., Nagib, H., 2009. INVITED PAPER: Criteria for assessing experiments in zero pressure gradient boundary layers. Fluid Dyn. Res. 41, http://dx.doi.org/10.1088/0169-5983/41/2/021404.

Choi, K.-S., DeBisschop, J.-R., Clayton, B.R., 1998. Turbulent boundary-layer control by means of spanwise-wall oscillation. AIAA J. 36 (7), 1157–1163. http://dx.doi.org/10.2514/2.526.

Di Cicca, G.M., Iuso, G., Spazzini, P.G., Onorato, M., 2002. Particle image velocimetry investigation of a turbulent boundary layer manipulated by spanwise wall oscillations. J. Fluid Mech. 467, 41–56. http://dx.doi.org/10.1017/S002211200200157X.

Diwan, S.S., Morrison, J.F., 2017. Spectral structure and linear mechanisms in a rapidly distorted boundary layer. Int. J. Heat Fluid Flow 67, 63–73. http://dx.doi.org/10.1016/j.ijheatfluidflow.2017.04.009, URL https://www.sciencedirect.com/science/article/pii/S0142727X16309249. Symposium on Experiments and Simulations in Fluid Dynamics Research.

Fukagata, K., Iwamoto, K., Kasagi, N., 2002. Contribution of Reynolds stress distribution to the skin friction in wall-bounded flows. Phys. Fluids 14 (11), L73–L76. http://dx.doi.org/10.1063/1.1516779.

Garcia-Mayoral, R., Jimenez, J., 2011. Drag reduction by riblets. Phil. Trans. R. Soc. A 369 (1940), 1412–1427. http://dx.doi.org/10.1098/rsta.2010.0359, arXiv:https://royalsocietypublishing.org/doi/pdf/10.1098/rsta.2010.0359. URL https://royalsocietypublishing.org/doi/abs/10.1098/rsta.2010.0359.

Gowree, E., Atkin, C., Gruppetta, S., 2015. A simple digital-optical system to improve accuracy of hot-wire measurements. Meas. Sci. Technol. 26, http://dx.doi.org/10.1088/0957-0233/26/9/095303.

Gowree, E., Jagadeesh, C., Atkin, C., 2019. Skin friction drag reduction over staggered three dimensional cavities. Aerosp. Sci. Technol. 84, 520–529.

Hinze, J.O., 1967. Secondary currents in wall turbulence. Phys. Fluids 10 (9), S122–S125. http://dx.doi.org/10.1063/1.1762429, arXiv:https://aip.scitation.org/doi/pdf/10.1063/1.1762429. URL https://aip.scitation.org/doi/abs/10.1063/1.1762429.

Hutchins, N., Choi, K.-S., 2002. Accurate measurements of local skin friction coefficient using hot-wire anemometry. Prog. Aerosp. Sci. 38 (4), 421–446. http://dx.doi.org/10.1016/S0376-0421(02)00027-1, URL http://www.sciencedirect.com/science/article/pii/S0376042102000271.

Hwang, D., Biesiadny, T., 1997. Experimental evaluation of penalty associated with micro-blowing for reducing skin friction. In: 36th AIAA Aerospace Sciences Meeting and Exhibit. p. 677.

Inoue, M., Pullin, D., Harun, Z., Marusic, I., 2013. LES of the adverse-pressure gradient turbulent boundary layer. Int. J. Heat Fluid Flow 44, 293–300. http://dx.doi.org/10.1016/j.ijheatfluidflow.2013.06.011, URL https://www.sciencedirect.com/science/article/pii/S0142727X13001410.

Iuso, G., Onorato, M., Spazzini, P.G., Di Cicca, G.M., 2002. Wall turbulence manipulation by large-scale streamwise vortices. J. Fluid Mech. 473, 23–58. http://dx.doi.org/10.1017/S0022112002002574.

Kadivar, M., Tormey, D., McGranaghan, G., 2021. A review on turbulent flow over rough surfaces: Fundamentals and theories. Int. J. Thermofluids 10, 100077. http://dx.doi.org/10.1016/j.ijft.2021.100077, URL https://www.sciencedirect.com/science/article/pii/S266620272100015X.

Kametani, Y., Fukagata, K., Örlü, R., Schlatter, P., 2015. Effect of uniform blowing/suction in a turbulent boundary layer at moderate Reynolds number. Int. J. Heat Fluid Flow 55, 132–142. http://dx.doi.org/10.1016/j.ijheatfluidflow.2015.05.019, Special Issue devoted to the 10th Int. Symposium on Engineering Turbulence Modelling and Measurements (ETMM10) held in Marbella, Spain on September 17-19, 2014.

Kendall, A., Koochesfahani, M., 2008. A method for estimating wall friction in turbulent wall-bounded flows. Exp. Fluids 44, 773–780. http://dx.doi.org/10.1007/s00348-007-0433-9.

Kline, S.J., Reynolds, W.C., Schraub, F.A., Runstadler, P.W., 1967. The structure of turbulent boundary layers. J. Fluid Mech. 30 (4), 741–773. http://dx.doi.org/10.1017/S0022112067001740.

Kornilov, V., 2015. Current state and prospects of researches on the control of turbulent boundary layer by air blowing. Prog. Aerosp. Sci. 76, 1–23. http://dx.doi.org/10.1016/j.paerosci.2015.05.001, URL https://www.sciencedirect.com/science/article/pii/S0376042115000329.

Leschziner, M.A., 2020. Friction-drag reduction by transverse wall motion – A review. J. Mech. 36 (5), 649–663. http://dx.doi.org/10.1017/jmech.2020.31.

Marusic, I., Chandran, D., Rouhi, A., fu, M., Wine, D., Holloway, B., Chung, D., Smits, A., 2021. An energy-efficient pathway to turbulent drag reduction. Nature Commun. 12, http://dx.doi.org/10.1038/s41467-021-26128-8.

Mathis, R., Hutchins, N., Marusic, I., 2009. Large-scale amplitude modulation of the small-scale structures in turbulent boundary layers. J. Fluid Mech. 628, 311–337. http://dx.doi.org/10.1017/S0022112009006946.

Monty, J., Harun, Z., Marusic, I., 2011. A parametric study of adverse pressure gradient turbulent boundary layers. Int. J. Heat Fluid Flow 32 (3), 575–585. http://dx.doi.org/10.1016/j.ijheatfluidflow.2011.03.004, URL https://www.sciencedirect.com/science/article/pii/S0142727X11000452. 8th International Symposium on Engineering Turbulence Modelling and Measurements, Marseille, France, June 9 to 11, 2010.

Mourão Bento, H.F., VanDercreek, C.P., Avallone, F., Ragni, D., Snellen, M., 2022. Lattice Boltzmann very large eddy simulations of a turbulent flow over covered and uncovered cavities. Phys. Fluids 34 (10), 105120. http://dx.doi.org/10.1063/5.0100001.

Nikuradse, J., 1930. Untersuchungen über turbulente Strömungen in nicht kreisförmigen Rohren. Ing.-Arch. 1, 306–332.

Örlü, R., Alfredsson, P.-H., 2012. On spatial resolution issues related to time-averaged quantities using hot-wire anemometry. Exp. Fluids 49, 101–110. http://dx.doi.org/10.1007/s00348-009-0808-1.

Patel, V.C., 1965. Calibration of the Preston tube and limitations on its use in pressure gradients. J. Fluid Mech. 23 (1), 185–208. http://dx.doi.org/10.1017/S0022112065001301.

Ricco, P., Skote, M., Leschziner, M.A., 2021. A review of turbulent skin-friction drag reduction by near-wall transverse forcing. Prog. Aerosp. Sci. 123.

Scarano, F., Jacob, M.C., Carbonneau, X., Gowree, E.R., 2022a. On the turbulent boundary layer over a flat plate at moderate Reynolds numbers. Phys. Fluids 34 (11), 115150. http://dx.doi.org/10.1063/5.0124498.

Scarano, F., Jacob, M.C., Gojon, R., Carbonneau, X., Gowree, E.R., 2022b. Modification of a turbulent boundary layer by circular cavities. Phys. Fluids 34 (6), 065134. http://dx.doi.org/10.1063/5.0091110.

Schlatter, P., Örlü, R., 2010. Assessment of direct numerical simulation data of turbulent boundary layers. J. Fluid Mech. 659, 116–126.

Silvestri, A., Ghanadi, F., Arjomandi, M., Cazzolato, B., Zander, A., 2017. Attenuation of sweep events in a turbulent boundary layer using micro-cavities. Exp. Fluids 58, http://dx.doi.org/10.1007/s00348-017-2345-7.

Soleimani, S., Eckels, S., 2021. A review of drag reduction and heat transfer enhancement by riblet surfaces in closed and open channel flow. Int. J. Thermofluids 9, 100053. http://dx.doi.org/10.1016/j.ijft.2020.100053, URL https://www.sciencedirect.com/science/article/pii/S2666202720300409.

Stroh, A., Schäfer, K., Frohnapfel, B., Forooghi, P., 2020. Rearrangement of secondary flow over spanwise heterogeneous roughness. J. Fluid Mech. 885, R5. http://dx.doi.org/10.1017/jfm.2019.1030.

Sullivan, P., Pollard, A., 1996. Coherent structure identification from the analysis of hot-wire data. Meas. Sci. Technol. 7 (10), 1498–1516. http://dx.doi.org/10.1088/0957-0233/7/10/020.

van Nesselrooij, M., Veldhuis, L.L.M., van Oudheusden, B.W., Schrijer, F.F.J., 2016. Drag reduction by means of dimpled surfaces in turbulent boundary layers. Exp. Fluids 57 (9), 142.

Vinuesa, R., Hosseini, S., Hanifi, A., Henningson, D., Schlatter, P., 2017. Pressure-gradient turbulent boundary layers developing around a wing section. Flow Turbul. Combust. 99, 613–641. http://dx.doi.org/10.1007/s10494-017-9840-z.

Viotti, C., Quadrio, M., Luchini, P., 2009. Streamwise oscillation of spanwise velocity at the wall of a channel for turbulent drag reduction. Phys. Fluids 21 (11), 115109. http://dx.doi.org/10.1063/1.3266945.